Flue gas adsorption by single-wall carbon nanotubes: A Monte Carlo study

M. I. Romero-Hermida,[1,2] J. M. Romero-Enrique,[3] V. Morales-Flórez,[2,4] and L. Esquivias[2,4]
[1]*Departamento de Química Física, Facultad de Ciencias, Universidad de Cádiz, Campus Río San Pedro s/n, 11510 Puerto Real, Spain*
[2]*Departamento de Física Condensada, Universidad de Sevilla, Av. Reina Mercedes s/n, 41012 Sevilla, Spain*
[3]*Departamento de Física Atómica, Molecular y Nuclear, Área de Física Teórica, Universidad de Sevilla, Av. Reina Mercedes s/n, 41012 Sevilla, Spain*
[4]*Instituto de Ciencia de Materiales de Sevilla (CSIC/US), Av. Américo Vespucio 49, 41092 Sevilla, Spain*

(Received 9 May 2016; accepted 2 August 2016; published online 19 August 2016)

Adsorption of flue gases by single-wall carbon nanotubes (SWCNT) has been studied by means of Monte Carlo simulations. The flue gas is modeled as a ternary mixture of N_2, CO_2, and O_2, emulating realistic compositions of the emissions from power plants. The adsorbed flue gas is in equilibrium with a bulk gas characterized by temperature T, pressure p, and mixture composition. We have considered different SWCNTs with different chiralities and diameters in a range between 7 and 20 Å. Our results show that the CO_2 adsorption properties depend mainly on the bulk flue gas thermodynamic conditions and the SWCNT diameter. Narrow SWCNTs with diameter around 7 Å show high CO_2 adsorption capacity and selectivity, but they decrease abruptly as the SWCNT diameter is increased. For wide SWCNT, CO_2 adsorption capacity and selectivity, much smaller in value than for the narrow case, decrease mildly with the SWCNT diameter. In the intermediate range of SWCNT diameters, the CO_2 adsorption properties may show a peculiar behavior, which depend strongly on the bulk flue gas conditions. Thus, for high bulk CO_2 concentrations and low temperatures, the CO_2 adsorption capacity remains high in a wide range of SWCNT diameters, although the corresponding selectivity is moderate. We correlate these findings with the microscopic structure of the adsorbed gas inside the SWCNTs. *Published by AIP Publishing.* [http://dx.doi.org/10.1063/1.4961023]

I. INTRODUCTION

The increase of the carbon dioxide content in the atmosphere since the start of the industrial revolution is a key cause of global warming, which is one of the most alarming worldwide environmental issues that mankind is currently facing.[1,2] Fossil-fueled power plants are responsible for roughly 40% of the total CO_2 emission, coal-fired plants being the main contributor.[3,4] Flue gases emitted from medium to large point sources are generally at or slightly above atmospheric pressure and fuel type, the chosen combustion system and operating conditions are the major factors affecting their composition.[5] Typically, the main component of the flue gas is N_2, as in pure air, with a molar fraction around 80% and other major components are CO_2, with a molar fraction typically between 3% and 15%, and O_2 with molar fraction between 5% and 15%. Water is usually also present in the flue gas, but it is possible to remove the moisture before the CO_2 sequestration process by using, for example, silica gel air dryers.[6] Finally, there are other minor components, such as SO_2, NO_x, and CO, as well as particulates in suspension.

Currently, there is an increasing interest in reducing and controlling the CO_2 concentration in the atmosphere, and it has been suggested that several combined strategies could achieve the stabilization of atmospheric CO_2 concentrations at around 500 ppm.[7] One of these technologies is carbon capture and storage (CCS), which involves not only CO_2 separation and fixation[3] and underground storage,[8] but also mineral sequestration.[9–11] As necessary starting steps in reversible capture and storage technologies and carbon reutilization, adsorption and membrane separation of CO_2 from flue gases have been deeply researched.[12] Many possible materials have been considered for CO_2 adsorption, including zeolites,[13,14] activated carbon,[15,16] metal-organic frameworks,[17,18] and single-wall carbon nanotubes (SWCNTs).[19] The latter have been identified as vessels for short-term reversible storage of CO_2 at ambient temperatures.[20] The performance of multiwalled carbon nanotubes to capture CO_2 from flue gases has been assessed in Refs. 6, 21, and 22, finding that after a suitable chemical modification they can show larger CO_2 adsorption capacities than zeolites or granular activated carbons. Additionally, it has been experimentally found that electrical resistance of carbon nanotubes is sensitive to the adsorption of gaseous molecules such as those released on burning of fossil fuels.[23,24] It was concluded that resistance decreases when oxidizing gas molecules adsorb on the surface, whereas adsorption of reducing gas molecules results in increasing it. These results, together with new experimental techniques, which allow controlled synthesis of monodisperse single-chirality SWCNT distributions,[25] make carbon nanotubes suitable for the development of innovative gas sensor technologies.

From a computational point of view, molecular simulations of the gas adsorption and separation by carbon nanotubes or related porous media have been extensively studied in the

literature.[20,26–41] Most of these simulation studies consider classical force fields, but *ab initio* calculations have also been reported.[19,27,42] The capacity of carbon nanotubes to adsorb pure CO_2 has been tested by computer simulations in isolated[19] and arrays of parallel SWCNTs,[20] as well as isolated[36] and parallel double-walled carbon nanotube bundles.[38,40] On the other hand, CO_2 separation by carbon nanotubes from mixtures has been studied in CO_2—CH_4 mixtures,[30,39] in presence of water[37] or in CO_2—N_2 mixtures.[33] This latter study, relevant for CO_2 capture from flue gases, studied the effect of pressure, temperature, and bulk gas composition on the CO_2 adsorption in SWCNTs with diameters between 8 and 10 Å. They find that the narrowest SWCNT (6,6) they considered presents an optimal CO_2 selectivity with respect to N_2 (of about 10) for $T = 300$ K, $p = 0.15$ MPa, and bulk CO_2 concentration $y_{CO_2} = 0.3$.[33]

Our goal in this paper is the molecular simulation study of the adsorption properties of flue gases under experimentally typical conditions by SWCNTs, paying special attention to their performance to capture CO_2. We will extend previous studies to a larger range of SWCNT diameters, spanning from around 7 Å, which can be obtained experimentally,[43] to 20 Å. On the other hand, we will consider the effect of the presence of oxygen in the flue gas. We will restrict ourselves to the study of the gas adsorption inside the nanotubes. Although the flue gas can be also adsorbed in the outer surfaces of the SWCNTs, its effect will depend not only on the nanotube geometry, but also in the aggregation properties, i.e., in the way the SWCNTs form bundles. This work will be performed by Monte Carlo computer simulations,[44,45] and thus dynamical properties such as diffusion cannot be considered. However, the Monte Carlo method is very suitable for the study of confined multicomponent fluids, where we do not know the adsorbed fluid compositions *a priori*. In this way we avoid those undesired finite-size effects that may arise in the simulation geometries. In order to characterize the effects of the carbon nanotube geometry, we have systematically studied the CO_2 adsorption properties of all the SWCNTs with a diameter smaller than 20 Å. The paper is organized as follows. In Section II we describe the molecular model of the flue gas and the carbon nanotubes. The simulation methods we will use are introduced in Section III. Our results will be presented and discussed in detail in Section IV, and we will end up our paper with the conclusions in Section V.

II. THE MODEL

We model the flue gas as a N_2, CO_2, and O_2 ternary mixture. Thus, the effect of the water or the minority components on its adsorption by SWCNT is not considered. The interactions between molecules are modeled by using the TraPPe force field.[46,47] Each molecule of the flue gas is considered to be rigid and linear, with fixed chemical bond distances d between neighbour atoms: $d = 1.1$ Å for N_2, $d = 1.21$ Å for O_2, and $d = 1.16$ Å for each C═O bond in CO_2. Furthermore, the two C═O bonds in each CO_2 molecule are always collinear. The molecular interactions are assumed to be pairwise, where the interaction between the i and j molecules is given by

$$v_2(i,j) = \sum_{\alpha\in i,\beta\in j}\left(4\epsilon_{\alpha\beta}\left[\left(\frac{\sigma_{\alpha\beta}}{r_{\alpha\beta}}\right)^{12} - \left(\frac{\sigma_{\alpha\beta}}{r_{\alpha\beta}}\right)^{6}\right] + \frac{q_\alpha q_\beta}{4\pi\epsilon r_{\alpha\beta}}\right), \tag{1}$$

where α and β represent the interaction centers of the i and j molecules, respectively. Each molecule has three interaction centers, associated to the atom nuclei of each molecule and, in the case of the diatomic molecules N_2 and O_2, the molecular center of mass (CM). Lennard-Jones potentials are associated to the atoms of each molecule (not to the molecular CMs). On the other hand, molecular electric quadrupolar moments are modeled by a distribution of point charges q_α associated to each interaction center α. In particular, two equal charges q are located at the atoms of the diatomic molecules, and an additional charge $-2q$ associated to their CM. For CO_2 molecules, two equal charges q are located at the oxygen atoms, and a charge $-2q$ at the carbon atom. Table I shows the relevant interaction parameters for the intermolecular interaction potential. For the parameters of the Lennard-Jones potential between dissimilar non-bonded atoms, the Lorentz-Berthelot combination rules are used

$$\sigma_{\alpha\beta} = \frac{\sigma_{\alpha\alpha}+\sigma_{\beta\beta}}{2}, \qquad \epsilon_{\alpha\beta} = \sqrt{\epsilon_{\alpha\alpha}\epsilon_{\beta\beta}}. \tag{2}$$

With respect to the SWCNTs, they are modeled as rigid, regular distributions of carbon atoms following the ideal structure of the carbon nanotube, i.e., defectless and infinite along the axial nanotube direction. This structure is obtained by wrapping a two-dimensional layer of graphite or graphene, which has a honeycomb structure with a bond distance between nearest-neighbour carbons of $a = 1.421$ Å, into a seamless cylinder. SWCNTs show periodic structures along its axis, characterized by the chiral indices (n,m), where the integer numbers n and m are the components of the chiral vector $\mathbf{C}_h$ in the basis vector of the honeycomb lattice. Under wrapping, $\mathbf{C}_h$ provides the perimeter of a carbon nanotube section. So, the geometric characteristics of ideal SWCNTs are uniquely determined by the carbon-carbon bond distance and the chiral indices.[48] In particular, the nanotube diameter

TABLE I. Intermolecular interaction parameters. Underlined atom symbols correspond to the interaction centers that the interaction parameter refers to. Lennard-Jones parameters for dissimilar atoms are obtained via the Lorentz-Berthelot combination rules Eq. (2). The interaction center charges q are in units of the electron charge $e = 1.6\times10^{-19}$ C. CM stands for the molecule center of mass.

	σ (Å)	ϵ/k_B (K)	q/e
$\underline{CO_2}$–$\underline{CO_2}$	2.8	27.0	0.70
$\underline{CO_2}$–$C\underline{O_2}$	3.05	79.0	−0.35
$\underline{N_2}$–$\underline{N_2}$	3.31	36.0	−0.482
$\underline{CM}(N_2)$–$\underline{CM}(N_2)$	...	...	0.964
$\underline{O_2}$–$\underline{O_2}$	3.013	49.048	−0.123
$\underline{CM}(O_2)$–$\underline{CM}(O_2)$	...	...	0.246

TABLE II. Parameters of the Steele potential between the SWCNT and the flue gas. Underlined atom symbols refer to the interaction center associated to the corresponding parameter.

	σ (Å)	ϵ/k_B (K)
C–$\underline{C}O_2$	3.11	27.0
C–$C\underline{O_2}$	3.16	45.6
C–$\underline{N_2}$	3.36	33.4
C–$\underline{O_2}$	3.19	37.6

d_t is given by

$$d_t = \frac{a\sqrt{3}}{\pi}\sqrt{n^2 + m^2 + nm}. \tag{3}$$

On the other hand, the wavelength T associated to the translational symmetry along the nanotube axis is given by $T = \sqrt{3}\pi d_t/d_R$, where d_t is given by Eq. (3) and d_R is the highest common divisor of $(2n + m, 2m + n)$. Without loss of generality, we can assume that $n \geq m$. If $m = 0$, SWCNTs are called zigzag nanotubes, and if $n = m$, SWCNTs are called armchair nanotubes. Otherwise, they are called chiral.

For the adsorbed flue gas, the presence of the SWCNT is twofold. First, it acts as a confining pore. On the other hand, the interactions between the SWCNT and the flue gas molecules can be expressed as an external field acting on the adsorbed flue gas. In the present work this interaction is modeled by the Steele potential[49–51]

$$v_1(i) = \sum_{\alpha \in i, \beta \in \mathrm{SWCNT}} 4\epsilon_{\alpha\beta}\left[\left(\frac{\sigma_{\alpha\beta}}{r_{\alpha\beta}}\right)^{12} - \left(\frac{\sigma_{\alpha\beta}}{r_{\alpha\beta}}\right)^{6}\right], \tag{4}$$

where α runs over the interaction centers of the flue gas adsorbed molecule i, and β labels the SWCNT carbon atoms. The parameters for the Steele potential are taken to be the same as for a fluid in contact with a flat graphite surface (see Table II). However, recent *ab initio* calculations of adsorbed gases on Schwarzite C_{168} show that the nanotube curvature may have an effect on the adsorption properties.[27]

III. METHODOLOGY

As mentioned in the Introduction, we will study the physisorption of flue gases inside SWCNT in thermodynamic equilibrium with a bulk reservoir. So, in a first step we will characterize the thermodynamic properties of the bulk flue gas, and in particular the chemical potentials for each species for a given temperature, pressure, and mixture compositions y_i. Although there are empirical equations of state which can provide these quantities, in the present work they will be evaluated by NpT Monte Carlo simulations. In addition, grand-canonical Monte Carlo simulations will be performed to check the accuracy of the NpT estimates. After that, we will study the flue gas adsorption inside SWCNTs via grand-canonical Monte Carlo simulations, using for each species the chemical potential obtained from the bulk simulations for the same temperature and pressure. In this way, the coexistence between the confined and the flue gas is ensured. In this work, we will restrict ourselves to the temperatures $T = 300$ K, 350 K, and 400 K, and as values of the pressure 1–4 atm. These values span the range considered by experimental studies of flue gas adsorption on multiwalled carbon nanotubes.[6] Now we present a summary of the simulation details.

A. Bulk simulations

Bulk Monte Carlo simulations are performed on cubic boxes subject to periodic boundary conditions, using the Metropolis algorithm. Lennard-Jones interactions are truncated at a cutoff distance $r_c = 8.5$ Å. The long-ranged character of the electrostatic interactions is handled by the use of the Ewald summation technique[52] with real space damping parameter $\alpha = 4$ and a maximum wave vector $k_{max} = 10\pi/L$ for the Fourier part.

In order to obtain the chemical potentials of each component of the flue gas, we performed NpT Monte Carlo simulations. The total number of molecules is set to $N = 1000$, of which 800 correspond to N_2 molecules ($y_{N_2} = 0.8$). In order to study the effect of the bulk CO_2 concentration of the flue gas on the adsorption, we have considered the cases $(N_{CO_2}, N_{O_2}) = (0, 200)$, $(50, 150)$, $(100, 100)$, $(150, 50)$, and $(200, 0)$, i.e., $(y_{CO_2}, y_{O_2}) = (0.00, 0.20)$, $(0.05, 0.15)$, $(0.10, 0.10)$, $(0.15, 0.05)$, and $(0.20, 0.00)$, respectively. We start from a configuration where the molecules are located at the sites of a simple cubic lattice of initial volume 2.7×10^7 Å^3. Each simulation typically consists of 55 000 Monte Carlo cycles, where the initial 5000 cycles are disregarded as an equilibration period, and averages are taken over the remaining cycles. Each Monte Carlo cycle consists of $N + 1$ trial movements, which in average correspond to N random translations and rotations of a molecule chosen also at random, and a box volume change (keeping its cubic shape), where the molecular positions are rescaled accordingly. The maximum molecular displacement is set to 100 Å, and the maximum angle rotation with respect to the original orientation is of 70°. Finally, maximum volume change is $V_0/2$, where V_0 is the current simulation box volume. With these values, the molecular movement acceptance ratio is about 99%, due to the low density of the flue gas under the considered conditions of temperature and pressure. On the other hand, the volume change acceptance ratio is about 20%. Different thermodynamic properties, such as the inner energy or the virial pressure, are obtained as run averages of their microscopic analogues. The chemical potentials of the flue gas species are obtained by Widom's test particle method.[53] In particular, the activity coefficient z_i of the i species is obtained as

$$z_i = \frac{e^{\beta\mu_i}}{\Lambda^3\Lambda_r} = \left\langle \frac{1}{4\pi(N_i + 1)} \int d\mathbf{r}_i \, d\omega_i \exp\left[-\sum_{j=1}^{N} \beta v_2(i,j)\right]\right\rangle^{-1}, \tag{5}$$

where $\Lambda = h/\sqrt{2\pi m k_B T}$ and $\Lambda_r = h^2/(4\pi^2 I k_B T)$, with m and I being the molecular mass and inertia moment, respectively. N_i is the number of particles of species i, v_2 is the pair potential Eq. (1), and $\langle \ldots \rangle$ corresponds to the thermal average.

In order to check the obtained values for the chemical potential from our NpT simulations, we also performed grand-canonical Monte Carlo simulations of the bulk flue gas. As in the NpT simulations, the simulation box is cubic, with a volume which, depending on the thermodynamic conditions, is between 8×10^6 Å^3 and 2.7×10^7 Å^3, in order to have an average total number of particles of about one thousand. We considered runs of typically 3×10^7 Monte Carlo steps after an equilibration period of 3×10^6 steps, starting from an empty box. In these simulations, a Monte Carlo step is trial insertion or deletion of a molecule. The species of the molecule is chosen randomly between those present in the flue gas with the same probability. Again, the low densities of the flue gas under the considered thermodynamic conditions lead to insertion and deletion acceptance ratios of around 99%. We use as an input of the chemical potentials the estimated values from the previous NpT simulations. As an output, we obtain the average mole fractions $y_i = \langle N_i \rangle / \langle N \rangle$, where N_i and N are the instantaneous values of the i-species number of particles and total number of particles, respectively. Comparison between these values and the input values of the corresponding NpT simulations provides an accuracy test for the activity coefficients.

B. Simulations in SWCNTs

Flue gases under confinement in SWCNTs have been studied by grand canonical Monte Carlo simulations, with the activity coefficients obtained from the bulk NpT simulations for the selected values of temperature, pressure, and bulk flue composition. In this way, the confined fluid will be in equilibrium with the corresponding bulk gas. The simulation procedure is similar to the one outlined above for the grand canonical Monte Carlo simulations of the bulk flue gas. However, now the simulation box is a cylinder of diameter d_t given by Eq. (3), and an axial length L_z which is a multiple of the wavelength T of the carbon nanotube. The integer number of proportionality is chosen in such a way that L_z is around 100 Å. Periodic boundary conditions are only considered along the nanotube axis direction, and the cylinder wall is impenetrable for the interaction centers of each molecule. In addition to the fluid-fluid interactions, the external potential Eq. (4) acts on each molecule. Finally, we do not use the Ewald summation to deal with the electrostatic interactions. The reason for this is that, at large distances, the electrostatic interactions are basically quadrupole-quadrupole interactions, which decay with the intermolecular distance as $1/r^5$. In the quasi-one dimensional situation we are considering, this potential decays fairly fast to zero as $r \to \infty$, so we can truncate it for distances larger than $L_z/2$.

We have considered a large set of narrow SWCNTs in the microporous range, i.e., with nominal diameters less than 2 nm: armchair nanotubes with $n = 6,7,\ldots,14$; zigzag nanotubes with $n = 9,\ldots,25$; and the chiral nanotubes (6,5), (7,4), (7,5), (7,6), (8,3), (8,4), (9,1), (9,3), (10,1), (10,5), (11,2), (12,4), (20,5), and (21,7). Their nominal nanotube diameters d_t span a range between 7.05 Å for the (9,0) nanotube, and 19.76 Å for the (21,7) nanotube. In each case, we compute the average mole fractions $x_i = \langle N_i \rangle / \langle N \rangle$ (note that in general they will differ from the bulk values y_i), the flue gas number density ρ, and the inner energy. From these data we evaluate the selectivity of the minority species relative to the flue gas major component N_2 as

$$S_{CO_2|N_2} = \frac{x_{CO_2}/x_{N_2}}{y_{CO_2}/y_{N_2}}, \qquad S_{O_2|N_2} = \frac{x_{O_2}/x_{N_2}}{y_{O_2}/y_{N_2}}. \tag{6}$$

In addition, we evaluate the i-species absolute adsorption capacity, q_i, in a (n,m) SWCNT as

$$q_i = \frac{P_{m_i}\langle N_i \rangle}{P_{at_C} N_C}, \tag{7}$$

where a is the carbon-carbon bond length in the SWCNT, $\langle N_i \rangle$ and N_C are the average number of particles of i-species in the confined flue gas and the number of carbon atoms in the simulated nanotube section, respectively, and P_{m_i} and P_{at_C} are the molecular weight of the i-species and the atomic weight of carbon, respectively. In order to compare to experimental results, the excess adsorption capacity q_i^{exc} must be evaluated by subtracting from $\langle N_i \rangle$ in Eq. (7) the contribution of the bulk fluid into the available volume

$$\langle N_i \rangle^{exc} = \langle N_i \rangle - n_i^b V_{free}, \tag{8}$$

where n_i^b is the bulk number density at the same thermodynamic conditions. The definition of the available volume V_{free} is somewhat ambiguous as the nanotube has soft boundaries. We estimate as the volume of a cylinder of the same length the simulation box along the CNT axis, and radius as $d_t/2 - \sigma_0$, where $\sigma_0 \approx (2.7 \pm 0.1)$ Å is estimated from the closest distance between the carbon nanotubes and the atoms which compose the flue gas molecules. In a similar way, an excess selectivity $S_{i|j}^{exc}$ is defined when considering the excess mole fractions of the adsorbed flue gas by subtracting the corresponding bulk contribution as in Eq. (8).

The isosteric heat of adsorption Q_{st} which characterizes the adsorption strength of the confined fluid by the adsorbate can be obtained as[54]

$$Q_{st} = x_{CO_2} Q_{CO_2} + x_{N_2} Q_{N_2} + x_{O_2} Q_{O_2}, \tag{9}$$

where the molar quantities Q_i are obtained as

$$Q_i \approx k_B T - \left(\frac{\partial \langle U \rangle}{\partial \langle N_i \rangle} \right)_{T,p,\langle N_{j \neq i} \rangle} \tag{10}$$

with U being the intermolecular energy of the adsorbed phase. The second term in the right-hand side of Eq. (10) can be obtained in simulation by the fluctuation formula

$$\left(\frac{\partial \langle U \rangle}{\partial \langle N_i \rangle} \right)_{T,p,\langle N_{j \neq i} \rangle} = \sum_j \left(\langle U N_j \rangle - \langle U \rangle \langle N_j \rangle \right) (\kappa^{-1})_{ij}, \tag{11}$$

where κ^{-1} is the inverse of the matrix κ, with elements $\kappa_{ij} \equiv \langle N_i N_j \rangle - \langle N_i \rangle \langle N_j \rangle$.[54]

We also evaluated structural properties such as the interaction center radial density profiles $n_\alpha(r)$ and axial pair

distribution functions $g_{\alpha\beta}(z)$, defined as

$$n_\alpha(r) = \frac{1}{2\pi r}\left\langle \sum_{m=1}^{N_\alpha} \delta(r_m - r)\right\rangle, \tag{12}$$

$$g_{\alpha\beta}(z) = \frac{L_z}{\langle N_\alpha\rangle\langle N_\beta\rangle}\left\langle \sum_{m=1}^{N_\alpha}{\sum_{n=1}^{N_\beta}}' \delta(|z_{mn}| - z)\right\rangle, \tag{13}$$

where δ is the Dirac delta, N_α is the total number of interaction centers of type α, r_m and z_m are the radial and axial coordinates of the interaction center m, and $z_{mn} \equiv z_m - z_n$. Finally, the prime in Eq. (13) means that we exclude the case $m = n$ if $\alpha = \beta$.

IV. RESULTS AND DISCUSSION

A. Bulk simulations

We have performed the bulk simulations of the flue gas following the procedure outlined in Sec. III. Table III shows the most relevant results from the NpT simulations for $p = 1$ atm. Similar results are obtained for higher pressures, although the virial pressure shows larger fluctuations for $p = 4$ atm. However, even in this case the standard deviation is less than 1%. Note that densities are similar to the corresponding one to pure air under normal conditions. The potential energy contribution to the inner energy per molecule, U, is small, which is consistent with the fact that the flue gas density is low. Actually, the obtained pair distribution functions between center of interactions show a microscopic structure which is typical for diluted gases.

Although in general we obtain accurate values for the thermodynamic properties of the flue gas, the activity coefficients obtained from the Widom insertion method show uncertainties of about 10%. However, the obtained values are consistent with the ideal gas limiting values $z_i \to N_i/\langle V\rangle$, with N_i being the number of molecules of the species i and V the box volume. This fact is not surprising because of the low density of the flue gas under the considered conditions. However, we have to confirm that the obtained values are appropriate for the grand-canonical simulations in the confined case. In order to check this, we performed grand-canonical simulations of the bulk flue gas, using the activity coefficients obtained from the NpT simulations. Table IV shows the grand-canonical simulation results for the same thermodynamic conditions considered for the simulations with results shown in Table III. The agreement between the data obtained by both procedures is excellent, validating the NpT simulation estimates for the activity coefficients.

B. Simulations in SWCNTs: Adsorption capacities, selectivities, and isosteric heat of adsorption

Grand-canonical Monte Carlo simulations of the flue gas confined in SWCNT are performed using the same conditions as those considered for the bulk gas simulations. In particular, we select the same values of temperature, pressure, and chemical potentials for all the species, ensuring in this way thermodynamic equilibrium between the bulk and the confined flue gas. The acceptance ratio of insertion/deletion of molecules differs from that corresponding to the bulk simulations. Furthermore, it depends on the nanotube diameter, spanning a range from 0.1%–2% for the narrowest SWCNT to 20%–25% for the widest nanotubes. We observe that for each species the adsorption capacity increases with the pressure. CO_2 and O_2 adsorption capacities decrease when the temperature is raised, but for N_2 this observation is only true for wide or very narrow SWCNT. However, for $y_{CO_2} = 0.15$ and 0.20, a non-monotonic behavior of the N_2 adsorption capacity with the temperature for large pressures and SWCNTs with intermediate diameters spanning from 8 Å to 10 Å is observed. Under these conditions, the N_2 adsorption capacity can be larger for $T = 350$ K than for $T = 300$ K.

We first analyze the adsorption properties of narrow and wide SWCNT. In order to characterize each scenario, we will consider as examples the SWCNT with chiral indices (9,1) ($d_t = 7.4$ Å) and (25,0) ($d_t = 19.58$ Å). The adsorption isotherms of each species are compared in Fig. 1 for bulk

TABLE III. NpT simulation results for the bulk gas with $p = 1$ atm. The 1σ statistical uncertainties, shown as subindexes, refer to the last decimal places.

p (atm)	T (K)	y_{CO_2}	ρ (kg/m^3)	U (kJ/mol)	p_{virial} (atm)	z_{CO_2} (10^{-6} Å^{-3})	z_{N_2} (10^{-5} Å^{-3})	z_{O_2} (10^{-6} Å^{-3})
1	300	0.00	1.155_1	-0.0057_1	1.000_1	...	1.93_{13}	4.9_3
1	300	0.05	1.181_{16}	-0.0063_3	1.002_{14}	1.24_{14}	1.9_2	3.7_4
1	300	0.10	1.202_2	-0.0070_1	0.999_2	2.44_{16}	1.94_{12}	2.44_{15}
1	300	0.15	1.227_2	-0.0077_1	0.999_1	3.6_3	1.94_{15}	1.23_{10}
1	300	0.20	1.252_2	-0.0083_1	1.000_2	4.9_4	1.94_{14}	...
1	350	0.00	0.990_1	-0.0050_1	1.000_1	...	1.66_9	4.2_2
1	350	0.05	1.010_1	-0.0054_3	0.999_1	1.0_6	1.65_7	3.11_{14}
1	350	0.10	1.030_1	-0.0059_1	0.999_1	2.1_2	1.65_{14}	2.09_{19}
1	350	0.15	1.051_1	-0.0063_1	0.999_1	3.1_5	1.6_4	1.0_3
1	350	0.20	1.072_2	-0.0069_1	0.999_1	4.2_4	1.66_{14}	...
1	400	0.00	0.866_1	-0.0042_1	1.000_1	...	1.46_{10}	3.6_3
1	400	0.05	0.883_{16}	-0.0047_1	0.999_1	0.93_7	1.45_9	2.74_{16}
1	400	0.10	0.902_1	-0.0050_1	1.000_1	1.82_9	1.45_7	1.82_8
1	400	0.15	0.920_1	-0.0054_1	0.999_1	2.7_3	1.46_{14}	0.93_9
1	400	0.20	0.938_1	-0.0058_1	1.000_1	3.7_4	1.46_{14}	...

TABLE IV. Grand-canonical simulation results for the bulk flue gas. The thermodynamic conditions are the same as those shown in Table III.

T (K)	z_{CO_2} (10^{-6} Å^{-3})	z_{N_2} (10^{-5} Å^{-3})	z_{O_2} (10^{-6} Å^{-3})	p_{virial} (atm)	ρ (kg/m^3)	y_{CO_2}	y_{N_2}
300	0.00	1.939	4.86	1.003_2	1.159_2	0.00	0.799_3
300	1.23	1.937	3.65	1.004_2	1.184_3	0.0508_2	0.798_4
300	2.44	1.936	2.44	1.003_3	1.208_3	0.1009_4	0.798_4
300	3.64	1.939	1.23	1.004_3	1.233_3	0.1503_6	0.798_4
300	4.86	1.942	0.00	1.006_2	1.259_2	0.2005_7	0.800_3
350	0.00	1.661	4.17	1.003_2	0.993_2	0.00	0.799_3
350	1.05	1.651	3.11	0.998_2	1.009_2	0.0509_2	0.799_4
350	2.08	1.654	2.09	1.000_2	1.031_2	0.1005_4	0.798_4
350	3.10	1.633	1.04	0.988_3	1.040_2	0.1516_6	0.798_4
350	4.17	1.663	0.00	1.005_2	1.078_2	0.2006_7	0.799_3
400	0.00	1.456	3.65	1.004_2	0.870_2	0.00	0.799_3
400	0.925	1.453	2.74	1.004_3	0.888_2	0.0509_2	0.798_4
400	1.82	1.445	1.82	0.998_3	0.901_2	0.1007_4	0.799_4
400	2.75	1.457	0.927	1.007_3	0.927_2	0.1508_6	0.798_4
400	3.67	1.464	0.00	1.011_2	0.948_2	0.2004_7	0.800_3

flue gases with CO_2 mole composition $y_{CO_2} = 0.15$, and the nanotube selectivities of CO_2 and O_2 for both SWCNTs are shown in Fig. 2. Similar results are obtained for other bulk flue gas compositions.

For narrow nanotubes, first we note that absolute and excess adsorption capacities are virtually identical, as it is shown in Fig. 1 for the (9,1) SWCNT. This is not surprising since the bulk phases have very low densities, and the free volume is very small. The adsorption isotherms are compatible with Type I (Langmuir) isotherms in the limited range of pressures which we have considered. Fig. 1 shows that CO_2 adsorption capacity is much larger than that corresponding to N_2, which in turn is one order of magnitude larger than for O_2. The latter observation is common for every SWCNT which we have considered. The CO_2 adsorption capacity increases with the bulk flue gas CO_2 mole fraction, whereas N_2 and O_2 adsorption capacities decrease as y_{CO_2} increases. Regarding the selectivities, Fig. 2 shows that the CO_2 selectivity for the (9,1) SWCNT is quite large. It decreases with the pressure, being larger for smaller temperatures. The O_2 selectivity, on the other hand, is quite insensitive to pressure, temperature, and bulk flue gas composition (within statistical uncertainties). These observations indicate that narrow SWCNTs have a strong affinity to CO_2 with respect to N_2 or O_2, these two being the latter components almost identical for adsorption properties.

For wide nanotubes, absolute and excess adsorption capacities show larger discrepancies, which do not exceed 10% for CO_2 adsorption, and 20% for the other components. The adsorption capacities are proportional to the pressure (Henry's law), although Type I behavior, which is typical for micropores, is expected for higher pressures. Fig. 1 shows

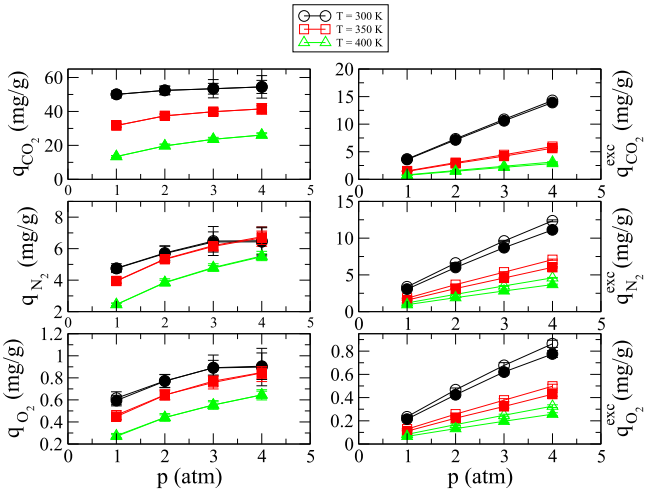

FIG. 1. Adsorption isotherms of CO_2 (top), N_2 (middle), and O_2 (bottom) for $y_{CO_2} = 0.15$, associated to the (9,1) (left) and (25,0) (right) SWCNT. Symbols correspond to different isotherms: circles for $T = 300$ K, squares for $T = 350$ K, and triangles for $T = 400$ K. Open symbols correspond to absolute adsorption capacities, and filled symbols to excess adsorption capacities. Lines only serve as eye guides.

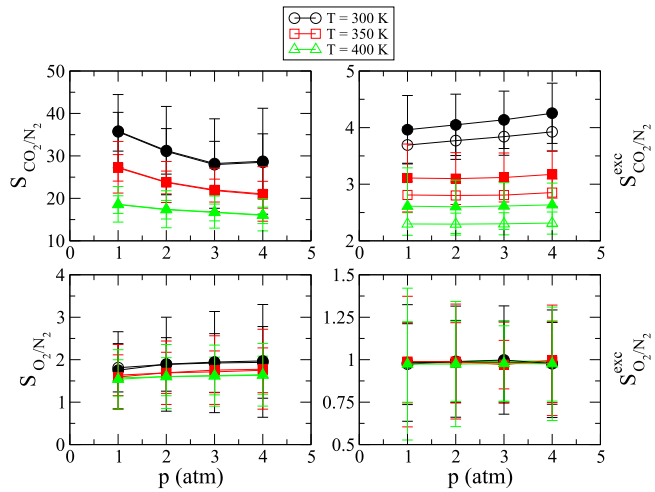

FIG. 2. CO_2 (top) and O_2 (bottom) selectivities for $y_{CO_2} = 0.15$ as functions of the pressure, associated to the (9,1) (left) and (25,0) (right) SWCNT. Symbols correspond to different isotherms: circles for $T = 300$ K, squares for $T = 350$ K, and triangles for $T = 400$ K. Open symbols correspond to absolute adsorption capacities, and filled symbols to excess adsorption capacities. Lines only serve as eye guides.

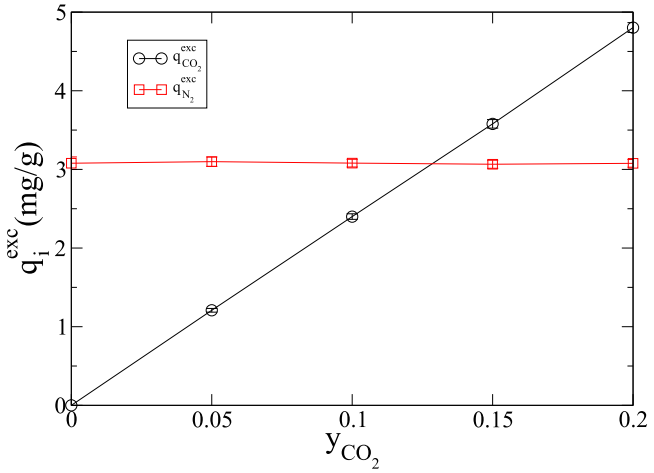

FIG. 3. CO_2 (circles) and N_2 (squares) excess adsorption capacities as a function of the bulk CO_2 composition y_{CO_2} for the (25,0) SWCNT at $T = 300$ K and $p = 1$ atm. Lines only serve as eye guides.

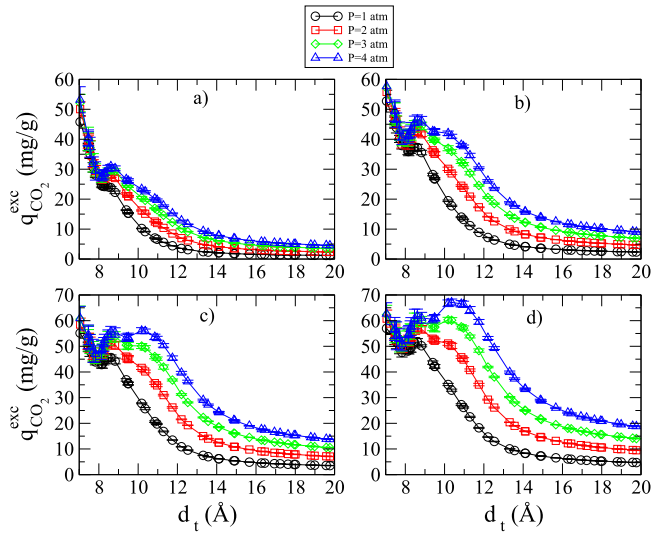

FIG. 4. CO_2 excess adsorption capacity as a function of the SWCNT diameter for $T = 300$ K and (a) $y_{CO_2} = 0.05$, (b) $y_{CO_2} = 0.10$, (c) $y_{CO_2} = 0.15$, (d) $y_{CO_2} = 0.20$. From bottom to top: $p = 1$ atm (circles), $p = 2$ atm (squares), $p = 3$ atm (diamonds), and $p = 4$ atm (triangles). Lines only serve as eye guides.

that for the (25,0) SWCNT the CO_2 adsorption capacity has decreased in a large proportion with respect to the (9,1) case, while for N_2 and O_2 remains in the same order of magnitude. We observe that N_2 is the preferentially adsorbed species for small bulk CO_2 mole fractions, but CO_2 adsorption capacity is larger than for N_2 when $y_{CO_2} = 0.2$, as shown in Fig. 3. On the other hand, the CO_2 selectivity of the (25,0) SWCNT is one order of magnitude smaller with respect to the (9,1) SWCNT, and now it increases with the pressure, being also a decreasing function of the temperature. In any case, the dependence on pressure of the CO_2 selectivity for the (25,0) SWCNT is weaker than for the (9,1) SWCNT. Again the O_2 selectivity is almost unity regardless the pressure, temperature and bulk flue gas composition (within statistical uncertainties). In fact, this observation is true for almost every SWCNT we have considered. The exception is the narrowest SWCNT (9,0), in which the O_2 selectivity shows an unusual behavior. Except for this case, O_2 selectivities have values between 0.7 and 2, and for nanotubes of diameter larger than 10 Å is approximately equal to 1.

The effect of the SWCNT geometry on the adsorption properties is shown in Figs. 4-8. We see that the nanotube diameter d_t is the main geometrical feature of the SWCNT for these properties. This is shown by their smooth dependence on d_t, and by the fact that different SWCNTs with different chirality indexes but the same diameter (such as the (6,5) and (9,1) SWCNTs) have, within the statistical uncertainties, the same adsorption properties, in agreement with previous results in the literature.[20] We focus on CO_2 adsorption capacity and selectivity, which are the most relevant properties for applications to CO_2 sequestration. Figs. 4–6 summarize the obtained results for CO_2 adsorption capacity. As we observed for the (9,1) and (25,0) SWCNTs, the adsorption capacity increases with the pressure or CO_2 mole fraction of the bulk flue gas, and in general when the temperature is decreased. As a function of the SWCNT diameter, the CO_2 adsorption capacity shows a peak for the narrowest SWCNT ($d_t = 7.05$ Å), and decreases steeply as the nanotube diameter increases, at least up to $d_t \approx 8$ Å. On the other hand, for wide nanotubes ($d_t \gtrsim 1$ nm), the CO_2 adsorption capacity decays smoothly with the nanotube diameter. For the intermediate range of SWCNT diameters, 8 Å $\lesssim d_t \lesssim$ 10 Å, we observe different scenarios when the thermodynamic conditions of the bulk flue gas are varied. For the highest temperatures $T = 400$ K, the CO_2 adsorption capacity is a monotonic decreasing function of d_t, except for narrowest SWCNT, where the extreme confinement can reduce its adsorption capacity for high temperatures (see Fig. 6). However, for high pressures this function displays a plateau for values of d_t between 8.1 and 8.7 Å. When the temperature is reduced to $T = 350$ K, two different scenarios are observed (see Fig. 5). When the bulk CO_2 mole fraction is $y_{CO_2} = 0.05$, the dependence of the adsorption capacity on the SWCNT diameter is similar to the case $T = 400$ K. As y_{CO_2} is increased, the CO_2 adsorption capacity develops a non-monotonic behavior with

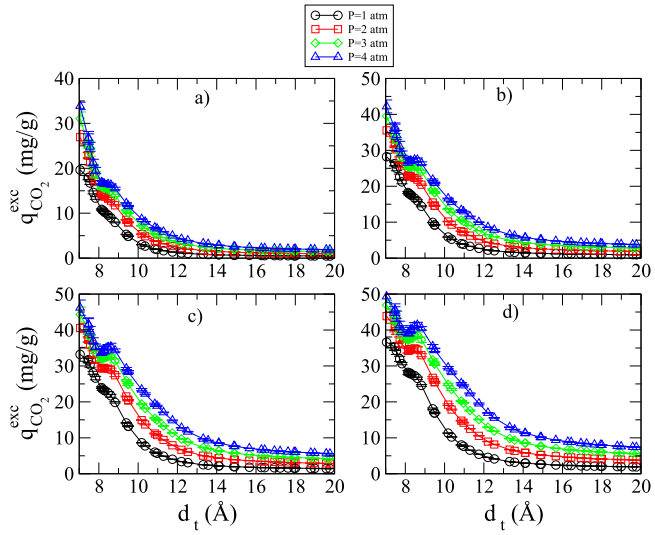

FIG. 5. The same as Fig. 4 for $T = 350$ K.

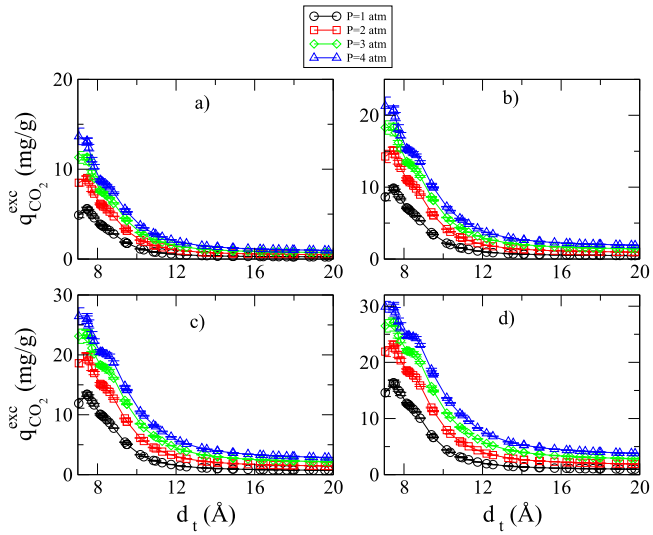

FIG. 6. The same as Fig. 4 for $T = 400$ K.

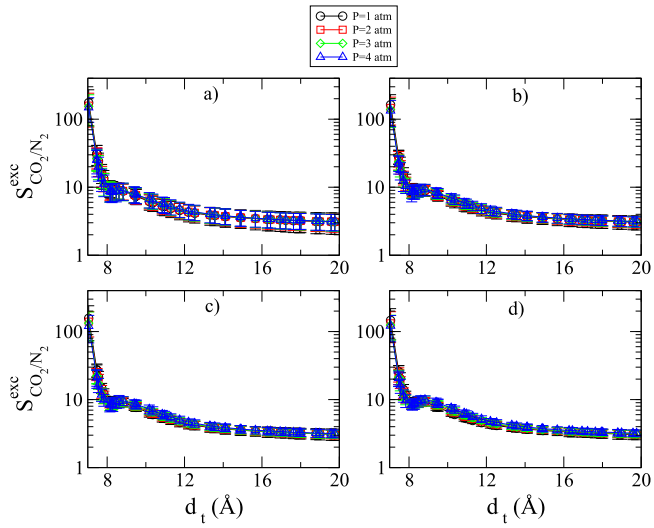

FIG. 8. The same as Fig. 7 for $T = 350$ K.

d_t, in such a way that it is an increasing function for d_t between 8.1 and 8.7 Å. This feature is even more evident in the lowest temperature, see Fig. 4. For $T = 300$ K, the maximum values of CO_2 adsorption capacity are between 60 and 70 mg/g, which are similar to those obtained for activated carbons at much higher values of y_{CO_2}.[6] Furthermore, for narrow SWCNTs the CO_2 adsorption capacity depends only weakly on the pressure. Finally, for high pressures and bulk CO_2 mole fractions, an additional maximum of the CO_2 adsorption capacity emerges at $d_t \approx 10.4$ Å, which can be even higher than that corresponding to the narrowest SWCNT for $p = 4$ atm and $y_{CO_2} = 0.2$.

Figs. 7–9 show the CO_2 selectivities with respect to N_2 as a function of the SWCNT diameter. We observe that the dependence on the pressure and y_{CO_2} is quite weak. As a function of d_t, a steep decay is observed for narrow SWCNTs, whereas for wide nanotubes it decreases smoothly with the SWCNT diameter. In all the cases there is an overall decrease of two orders of magnitude for the selectivity, being about 100 for the narrowest SWCNT, and of order of unity for wide nanotubes (note the semi-log scales in these figures). As it happened for the CO_2 adsorption capacity, at the highest temperature the dependence of S_{CO_2/N_2} on d_t displays a plateau for d_t between 8.1 and 8.7 Å, from which a local maximum emerges as the temperature decreases and/or y_{CO_2} increases.

Finally, the isosteric heat of adsorption shows a relatively small dependence on the thermodynamic properties of the bulk flue gas. The pressure dependence is more evident for the lowest temperature $T = 300$ K. Fig. 10 shows that it decays monotonically with the SWCNT diameter from about 45 kJ/mol for the narrowest nanotube to about 12 kJ/mol for the widest one. These values are about one order of magnitude above the thermal energy or the typical fluid-fluid interactions (see Table I). This fact, together with the relative insensitivity to the thermodynamic properties, indicates that

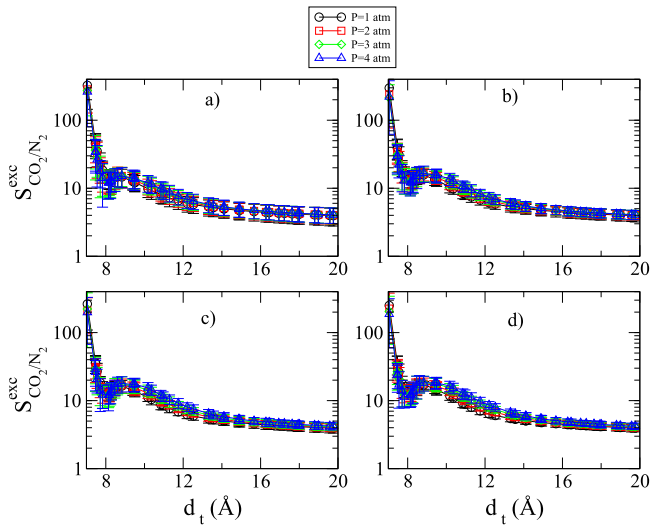

FIG. 7. CO_2 excess selectivity with respect to N_2 as a function of the SWCNT diameter for $T = 300$ K and (a) $y_{CO_2} = 0.05$, (b) $y_{CO_2} = 0.10$, (c) $y_{CO_2} = 0.15$, (d) $y_{CO_2} = 0.20$. From bottom to top: $p = 1$ atm (circles), $p = 2$ atm (squares), $p = 3$ atm (diamonds), and $p = 4$ atm (triangles). Lines only serve as eye guides.

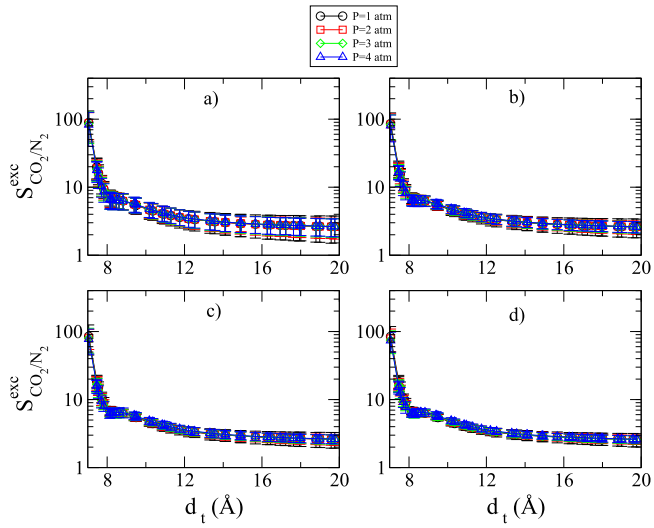

FIG. 9. The same as Fig. 7 for $T = 400$ K.

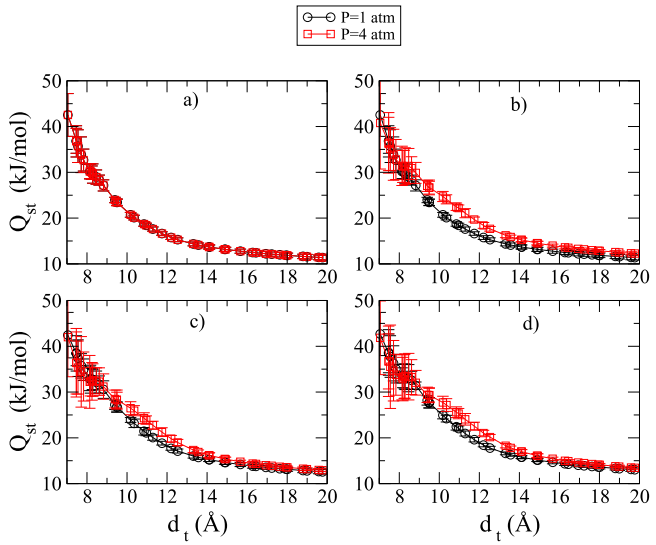

FIG. 10. Isosteric heat of adsorption as a function of the SWCNT diameter for $T = 300$ K and (a) $y_{CO_2} = 0.05$, (b) $y_{CO_2} = 0.10$, (c) $y_{CO_2} = 0.15$, (d) $y_{CO_2} = 0.20$. Circles correspond to $p = 1$ atm (circles) and squares to $p = 4$ atm. Lines only serve as eye guides.

the physisorption of the flue gas under the thermodynamic conditions we are considering is mainly controlled by the adsorbent-adsorbate interactions. Furthermore, this is also suggested by the fact that the isosteric heat can be estimated by $k_BT - \langle U\rangle/\langle N\rangle$ for most of the cases we have considered. Fluid-fluid interactions will have a relatively larger impact in the intermediate range of SWCNT diameters. We will come back to this point later.

C. Simulations in SWCNTs: Microscopic structure

From the results in Subsection IV B we conclude that the adsorption properties in SWCNT show different behaviors for narrow and wide nanotubes, with a transition between these regimes for SWCNTs with diameters between 8.1 and 8.7 Å. In order to understand this, we have studied the microscopic structure of the confined flue gas for the (9,1), (6,6), and (25,0) SWCNTs, corresponding to the narrow, intermediate, and wide cases. Results will be shown for $T = 300$ K, and $p = 1$ atm, although similar conclusions are found for different thermodynamic conditions.

Fig. 11 shows typical molecular configurations of the confined flue gas. In the (9,1) and (6,6) SWCNT, we observe that the particle density is larger than that corresponding to the bulk gas. Furthermore, the number of CO_2 molecules exceeds the number of N_2 molecules, and in these particular configurations no O_2 molecules are present. However, we see some differences between them: in the (9,1) SWCNT the CO_2 molecules are oriented along the nanotube axis, whereas their orientations are distributed more randomly in the (6,6) SWCNT. In the (25,0) SWCNT, the configuration is completely different: the particle density is much smaller, and molecules are preferentially localized close to the nanotube wall.

In order to quantify these observations, the number density profiles corresponding to the α atom, $n_\alpha(\mathbf{r})$, are shown

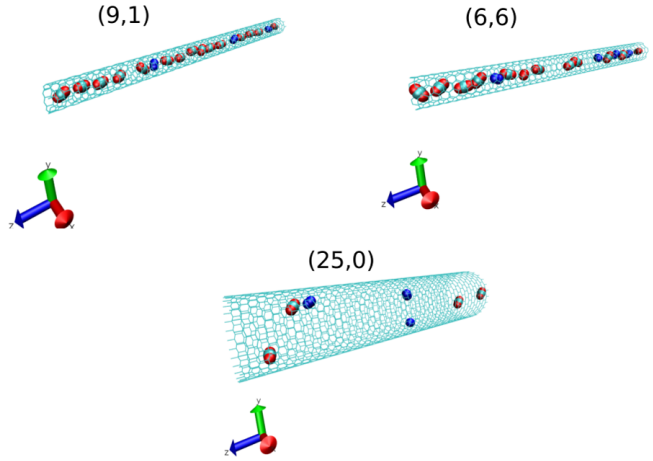

FIG. 11. Typical snapshots for the confined flue gas inside the (9,1), (6,6), and (25,0) SWCNTs. The bulk flue gas conditions are $p = 1$ atm, $T = 300$ K, and $y_{CO_2} = 0.10$. Triatomic molecules represent CO_2 and the diatomic molecules to N_2 (in these configurations there are no O_2 molecules). The network shows the positions of the carbon atoms in the SWCNT.

in Figs. 12–14 for the (9,1), (6,6), and (25,0) SWCNTs, respectively. We suppose that these functions only depend on the radial coordinate r with respect to the nanotube axis, which is a reasonable assumption as the nanotube inner surface is not very rough. Note that these profiles are non-zero only for values of $r \lesssim d_t/2 - \sigma_0$, where $\sigma_0 \approx 2.7$ Å $\sim \sigma_{\alpha C} \sim 3$ Å (see Table II). This is because the atoms of the flue gas molecules cannot be at a distance closer than $\sigma_{\alpha C}$ to any nanotube carbon, which are located on a cylinder of nominal radius, $d_t/2$. First, we note that for each SWCNT the CO_2 local densities increase with the bulk CO_2 mole fraction y_{CO_2}, whereas the N_2 and O_2 densities decrease. In Fig. 12 we see that all the density profiles show maxima at or near $r = 0$. Carbon atom densities from CO_2 show a clear peak at

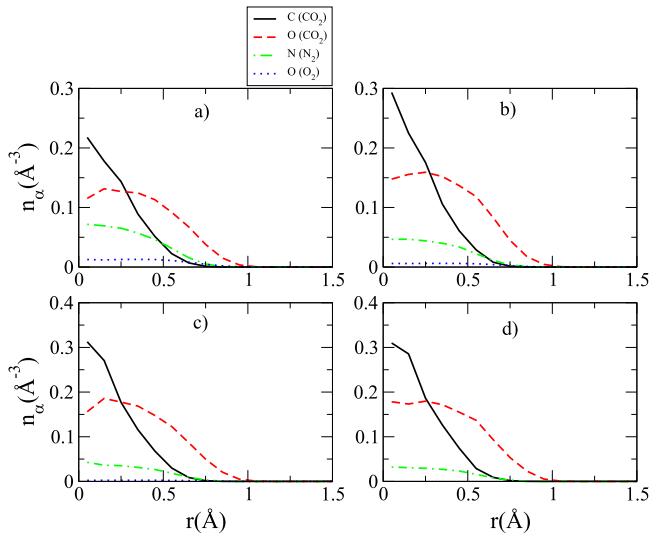

FIG. 12. Number density profiles $n_\alpha(r)$ of the atom α as a function of the radial coordinate r: continuous lines for C from CO_2, dashed lines for O from CO_2, dotted-dashed lines for N from N_2, and dotted lines for O from O_2. The flue gas is confined inside the (9,1) SWCNT, and it is in thermodynamic equilibrium with a bulk flue gas at $p = 1$ atm, $T = 300$ K and (a) $y_{CO_2} = 0.05$, (b) $y_{CO_2} = 0.10$, (c) $y_{CO_2} = 0.15$, and (d) $y_{CO_2} = 0.20$.

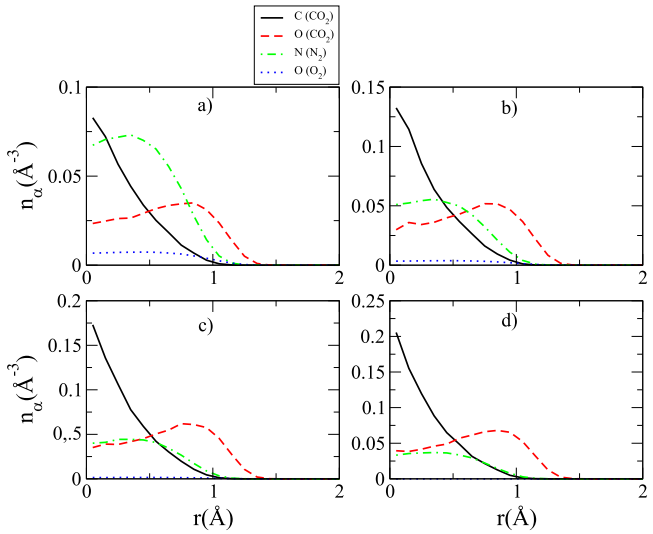

FIG. 13. The same as Fig. 12 for the flue gas confined inside the (6,6) SWCNT.

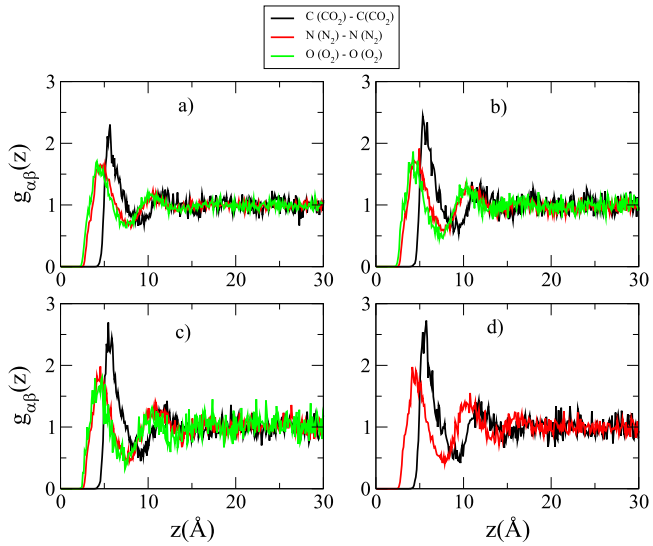

FIG. 15. Radial distribution functions $g_{\alpha\beta}(z)$ for the confined flue gas in the (9,1) SWCNT: black lines correspond to $\alpha = \beta =$ C (CO_2), red/dark grey to $\alpha = \beta =$ N, and green/light grey lines to $\alpha = \beta =$ O (CO_2). The bulk flue gas thermodynamic conditions are $p = 1$ atm, $T = 300$ K and (a) $y_{CO_2} = 0.05$, (b) $y_{CO_2} = 0.10$, (c) $y_{CO_2} = 0.15$, (d) $y_{CO_2} = 0.20$.

$r = 0$, but nitrogen and O_2 oxygen density profiles are quite broad in the accessible volume, although they still have a local maximum at $r = 0$. Finally, the CO_2 oxygen density profiles are also broad and display maxima which are slightly shifted from the origin. This means that CO_2 molecules are not perfectly aligned parallel to the nanotube. However, these features confirm our previous statement that in the (9,1) SWCNT molecules orient preferentially along the nanotube axial direction. No additional structures are observed. For the (6,6) SWCNT, we observe a change in the density profiles (see 13). Carbon density profiles show that CO_2 carbon atoms are still located preferentially at $r = 0$. However, nitrogen and CO_2 oxygen density profiles have maxima close to the nanotube inner surface. In any case, these density profiles are still quite broad. Finally, Fig. 14 plots the density profiles corresponding to the (25,0) SWCNT. In this case, the local densities are much smaller than in the previous nanotubes.

The inner region shows a density profile practically flat, which is approximately equal to the corresponding bulk density. On the other hand, every atomic species shows a maximum close to the nanotube inner surface. CO_2 adsorption is still enhanced with respect to the bulk case, but not so strongly as in (9,1) and (6,6) SWCNTs.

Finally, we characterized the correlation between molecules with the axial distribution functions. Figs. 15–17 show some of these functions for the confined flue gas in the (9,1), (6,6), and (25,0), respectively. We first note that, for each nanotube, they are quite insensitive to the bulk CO_2 mole fraction. In the (9,1) and (6,6) nanotubes the axial distribution functions show similar features to the radial distribution functions of a bulk liquid (i.e., a dense fluid),

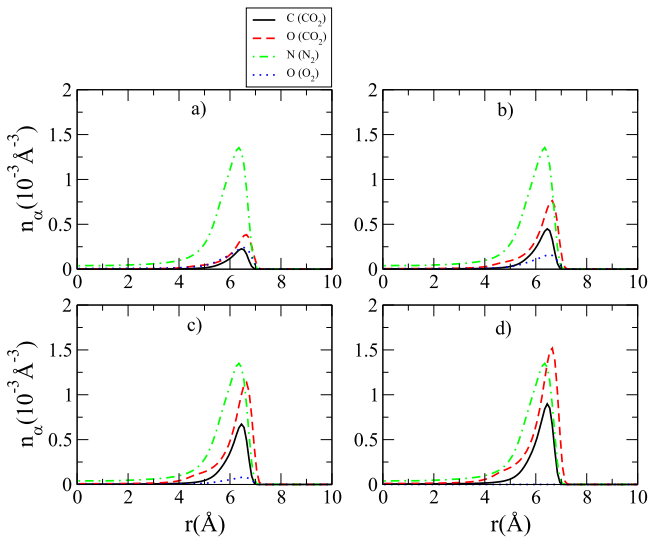

FIG. 14. The same as Fig. 12 for the flue gas confined inside the (25,0) SWCNT.

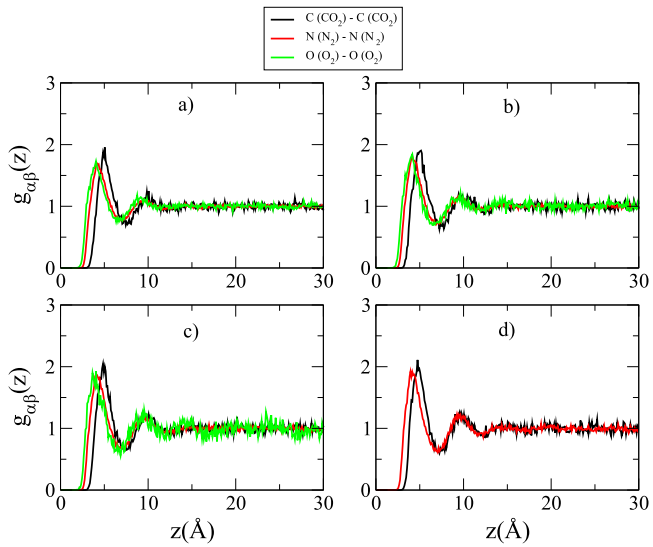

FIG. 16. The same as Fig. 15 for the flue gas confined inside the (6,6) SWCNT.

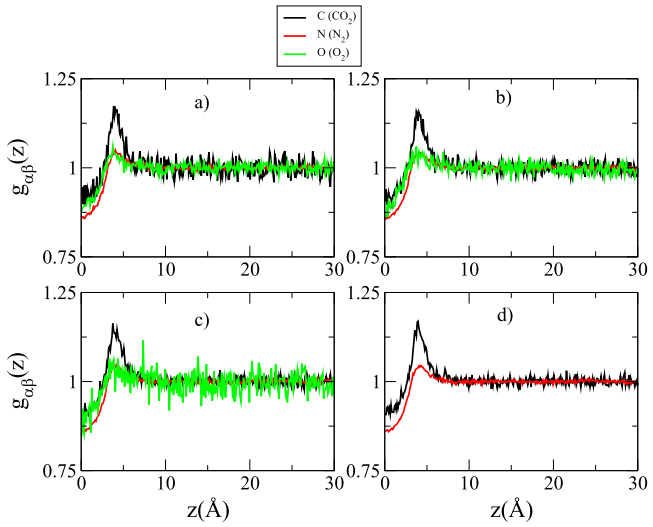

FIG. 17. The same as Fig. 15 for the flue gas confined inside the (25,0) SWCNT.

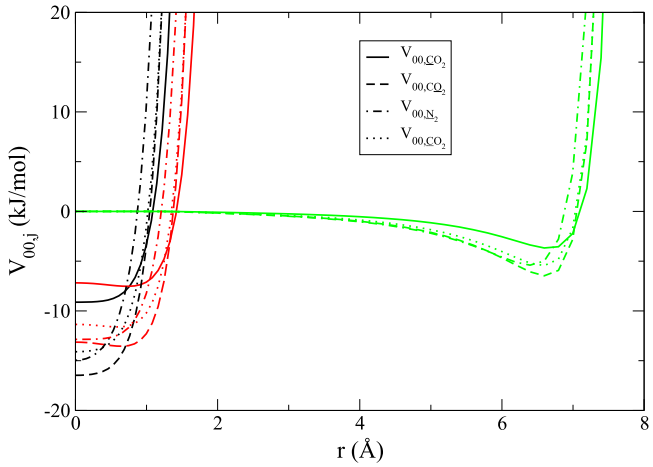

FIG. 18. SWCNT-atom potentials $V_{00,j}$, for the SWCNT with indexes (9,1) (black lines), (6,6) (red lines) and (25,0) (green lines) SWCNTs. The atom j is the carbon from CO_2 for continuous lines, the oxygen from CO_2 for the dashed lines, the nitrogen from N_2 for the dot-dashed lines and the oxygen from O_2 for the dotted lines.

with a depletion region for $z < \sigma_{\alpha\beta}$ and damped oscillations around 1 as z increases. In this sense, the confined flue gas in narrow and intermediate SWCNTs is a quasi-one dimensional liquid. We note the first peak of the axial distribution functions between CO_2 carbons is shifted to smaller values of z as the nanotube diameter increases. The reason for this displacement is twofold. First, an increase in the SWCNT diameter allows a closer approximation between carbons in the z direction, even when CO_2 multiple occupancy is not permitted at the same nanotube cross-section. On the other hand, we have previously seen that as the nanotube is wider, the CO_2 molecules orient more randomly, allowing carbons to be closer. For the (25,0) SWCNT, the axial distribution functions are quite different. First, it takes non-zero values at $z = 0$, since now multiple occupancy at the same cross-section is allowed. After the depletion region, these functions show a local maximum and for larger values decays very fast to 1. These features are characteristic of a gas (i.e., a fluid with low density).

D. Energetic analysis

We can rationalize these findings with energetic arguments. The results for the isosteric heat of adsorption indicate that the flue gas adsorption is mainly controlled by the nanotube-flue gas interactions. Each molecular interaction center j (i.e., atom) feels a potential $V_j(\mathbf{r})$ which is the superposition of the Lennard-Jones potential between the center and the carbon atoms which constitute the SWCNT. This potential will depend on the cylindrical coordinates of the interaction center (r,θ,z), and it can be expanded as a 2D Fourier series

$$V_j(r,\theta,z) = \sum_{n=-\infty}^{\infty}\sum_{m=-\infty}^{\infty} V_{nm,j}(r)e^{in\theta}e^{im\frac{z}{T}}, \qquad (14)$$

where T is the SWCNT period along the z axis. As mentioned previously, we find that this potential has approximately cylindrical symmetry, so its behaviour is controlled by $V_{00,j}(r)$, which is the average over θ and z of $V_j(\mathbf{r})$ at a fixed value of r. These functions have different shapes depending on the SWCNT diameter, as it can be seen in Fig. 18. For narrow nanotubes, the nanotube-atom interaction potential has a deep minimum at $r = 0$, so molecules have a tendency to locate at the nanotube axis and parallel to it. This fact explains why intermolecular interactions are less important than the potential between the carbon nanotube and the adsorbed gas despite the high density of the confined flue gas, as the minimum interaction energies between molecules in nose-to-tail configurations are of order of −1 kJ/mol (see Table I). Furthermore, the nanotube interacts more strongly with CO_2, which is a triatomic molecule, than with the diatomic molecules N_2 or O_2 (see Table II). As the SWCNT-fluid potential has a potential well shape, its effect, in addition to confining the flue gas molecules in the nanotube, will be to introduce a shift in the chemical potential of the j species of order of $-V_{00,j}(0)$. This can be easily justified if we write the grand-partition function assuming that there are no interactions between the confined flue gas molecules and the SWCNT-fluid potential is approximated by a square well with depth $-V_{00,j}(0)$. Consequently, under confinement the activity coefficients of all species are effectively larger than in bulk, being this increase larger for the CO_2 than for the other components. Thus, the number densities in the confined flue gas are larger than in bulk, leading to their liquid-like character. On the other hand, CO_2 concentration in the confined flue gas is much larger than in bulk at the same activity coefficients, so large CO_2 adsorption capacities and selectivities are obtained. Finally, the relative concentration of O_2 with respect to N_2 is close to the bulk value as their interaction potentials with the SWCNT are similar (see Table II). As a consequence, the O_2 selectivity is of order of 1.

As the nanotube diameter increases, the atom-nanotube interaction potentials become flatter inside the nanotube, and above some threshold the interaction potentials change their shape: they show a maximum at $r = 0$, whereas the potential minima are shifted towards values of $r > 0$, with a

displacement which is approximately linear with the nanotube diameter. In addition, the potential energy at these minima decreases as the nanotube diameter increases to values corresponding to a single graphene sheet, which is about one third of the value for the narrowest nanotube. This explains that the different density profiles become broader in the accessible volume for intermediate diameters, and that for wide nanotubes, the density profiles are practically equal to the bulk value inside the nanotube except close to the inner surface, where the density is enhanced by the interactions with the SWCNT in a similar way for the flue gas in contact with a flat sheet of graphene. The role of the fluid-fluid interactions is again negligible for wide SWCNTs, since the particle densities are relatively small. However, this may not be the case in the intermediate range of SWCNT diameters, where densities are higher, particles can approach closer, and the nanotube-fluid interactions are smaller. So, the peculiar behavior of the adsorption properties observed for the intermediate range of SWCNT diameters may be the result that fluid-fluid interactions may mitigate the reduction of nanotube-fluid interactions. We note that fluid-fluid interactions are stronger in CO_2 than in N_2 or O_2, which may explain why CO_2 adsorption is amplified at low temperatures and high pressures and bulk CO_2 concentrations.

V. CONCLUSIONS

In this paper the adsorption of flue gases inside isolated SWCNTs has been investigated by Monte Carlo simulations. We have focussed on the effect that the flue gas CO_2 bulk composition and the nanotube geometry has on the CO_2 capture. We find that the SWCNT geometric feature that controls the CO_2 adsorption properties is its diameter, being almost insensitive to its chirality. Our results show that SWCNTs with diameters around 7 Å show high CO_2 adsorption capacities and selectivities not observed in previous studies,[33] but these quantities decrease abruptly as the nanotube diameter increases. On the other hand, wide SWCNTs show much smaller adsorption capacities and selectivities, which decrease smoothly as the nanotube diameter increases. The microscopic properties of the confined flue gas explain the different behavior in each scenario. In narrow nanotubes the confined fluid has liquid-like characteristics with a CO_2 composition much larger than in bulk. On the other hand, for wide nanotubes the confined flue gas density and composition are almost equal to the bulk except in a monolayer close to the inner nanotube surface. In any case, the enhancement of the densities and CO_2 composition in this monolayer is not so strong as for narrow SWCNTs. The borderline between these two scenarios corresponds to nanotubes with diameters between 8 and 10 Å. For this intermediate range of SWCNT diameters, CO_2 adsorption properties have a strong dependence on the bulk gas conditions. So, for high bulk CO_2 concentrations and low temperatures, CO_2 adsorption capacity is high in a wide range of SWCNT diameters (specially at high pressures), but the corresponding selectivity is moderate.

Although our study is restricted to the adsorption properties inside ideal SWCNTs, our results will be relevant to design carbon-nanotube-based materials with high CO_2 adsorption capacities and selectivities. For example, CO_2 adsorption properties may be improved by considering bundles of parallel SWCNTs, since the interstices between nanotubes may act as additional pores which select CO_2 over the other flue gas species. However, it is beyond the scope of this paper to explore these options. The main conclusion of our paper is that, for practical applications, narrow SWCNTs are good candidates for materials to capture and store CO_2 from a flue gas, specially for low temperatures, high pressures, and high bulk CO_2 concentrations.

ACKNOWLEDGMENTS

M.I.R.-H., V.M.-F., and L.E. acknowledge financial support from the Spanish Ministerio de Economía y Competitividad through Grant No. MAT2013-42934-R, co-funded by the EU FEDER. V.M.-F. also acknowledges a postdoctoral grant from V Plan Propio de Investigacin of the Universidad de Sevilla (Spain). J.M.R.-E. acknowledges financial support from the Spanish Ministerio de Economía y Competitividad through Grant No. FIS2012-32455, co-funded by the EU FEDER, and the Portuguese Foundation for Science and Technology under Contract No. EXCL/FIS-NAN/0083/2012.

[1]Intergovernmental Panel on Climate Change (IPCC), *Climate Change 2013: The Physical Science Basis* (Cambridge University Press, Cambridge, 2013).
[2]J. Hansen, P. Kharecha, M. Sato, V. Masson-Delmotte, F. Ackerman, D. J. Beerling, P. J. Hearty, O. Hoegh-Guldberg, S. L. Hsu, C. Parmesan, J. Rockstrom, E. J. Rohling, J. Sachs, P. Smith, K. Steffen, L. Van Susteren, K. von Schuckmann, and J. C. Zachos, PLoS One **8**, e81648 (2013).
[3]M. Mikkelsen, M. Jorgensen, and F. C. Krebs, Energy Environ. Sci. **3**, 43 (2010).
[4]Intergovernmental Panel on Climate Change (IPCC), *Special Report on Carbon Dioxide Capture and Storage* (Cambridge University Press, Cambridge, 2005).
[5]S. Chakravarti, A. Gupta, and B. Hunek, "Advanced technology for the capture of carbon dioxide from flue gases," Proceedings of the First National Conference on Carbon Sequestration, Washington, DC, 2001.
[6]F. S. Su, C. S. Lu, W. F. Cnen, H. L. Bai, and J. F. Hwang, Sci. Total Environ. **407**, 3017 (2009).
[7]S. Pacala and R. Socolow, Science **305**, 968 (2004).
[8]P. Jaramillo, W. M. Griffin, and S. T. McCoy, Environ. Sci. Technol. **43**, 8027 (2009).
[9]I. M. Power, A. L. Harrison, G. M. Dipple, S. A. Wilson, P. B. Kelemen, M. Hitch, and G. Southam, Rev. Mineral. Geochem. **77**, 305 (2013).
[10]V. Morales-Florez, A. Santos, and L. Esquivias, J. Sol-Gel Sci. Technol. **59**, 417 (2011).
[11]V. Morales-Florez, A. Santos, I. Romero-Hermida, and L. Esquivias, Chem. Eng. J. **265**, 194 (2015).
[12]X. Q. Lu, D. L. Jin, S. X. Wei, Z. J. Wang, C. H. An, and W. Y. Guo, J. Mater. Chem. A **3**, 12118 (2015).
[13]W. H. Gao, D. Butler, and D. L. Tomasko, Langmuir **20**, 8083 (2004).
[14]R. V. Siriwardane, M. S. Shen, and E. P. Fisher, Energy Fuels **19**, 1153 (2005).
[15]R. V. Siriwardane, M. S. Shen, E. P. Fisher, and J. A. Poston, Energy Fuels **15**, 279 (2001).
[16]J. Przepiórski, M. Skrodzewicz, and A. W. Morawski, Appl. Surf. Sci. **225**, 235 (2004).
[17]J. R. Li, Y. G. Ma, M. C. McCarthy, J. Sculley, J. M. Yu, H. K. Jeong, P. B. Balbuena, and H. C. Zhou, Coord. Chem. Rev. **255**, 1791 (2011).
[18]O. Shekhah, Y. Belmabkhout, Z. J. Chen, V. Guillerm, A. Cairns, K. Adil, and M. Eddaoudi, Nat. Commun. **5**, 4228 (2014).
[19]M. Cinke, J. Li, C. W. Bauschlicher, Jr., A. Ricca, and M. Meyyapan, Chem. Phys. Lett. **376**, 761 (2003).
[20]P. Kowalczyk, S. Furmaniak, P. A. Gauden, and A. P. Terzyk, J. Phys. Chem. C **114**, 21465 (2010).

[21]C. Y. Lu, H. L. Bai, B. Wu, F. S. Su, and J. F. Hwang, Energy Fuels **22**, 3050 (2008).
[22]S. C. Hsu, C. S. Lu, F. S. Su, W. T. Zeng, and W. F. Chen, Chem. Eng. Sci. **65**, 1354 (2010).
[23]M. Mittal and A. Kumar, Sens. Actuators, B **203**, 349 (2014).
[24]A. Star, T. R. Han, V. Joshi, J. C. P. Gabriel, and G. Grüner, Adv. Mater. **16**, 2049 (2004).
[25]J. R. Sanchez-Valencia, T. Dienel, O. Gröning, I. Shorubalko, A. Mueller, M. Jansen, K. Amsharov, P. Ruffieux, and R. Fasel, Nature **512**, 61 (2014).
[26]J. Jiang and S. I. Sandler, Langmuir **19**, 5936 (2003).
[27]J. Jiang and S. I. Sandler, J. Am. Chem. Soc. **127**, 11989 (2005).
[28]A. I. Skoulidas, D. S. Sholl, and J. K. Johnson, J. Chem. Phys. **124**, 054708 (2006).
[29]G. Arora and S. I. Sandler, Fluid Phase Equilib. **259**, 3 (2007).
[30]L. L. Huang, L. Z. Zhang, Q. Shao, L. H. Lu, X. H. Lu, S. Y. Jiang, and W. F. Shen, J. Phys. Chem. C **111**, 11912 (2007).
[31]G. P. Lithoxoos, A. Labropoulos, L. D. Peristeras, N. Kanellopoulos, J. Samios, and amd I. G. Economou, J. Supercrit. Fluids **55**, 510 (2010).
[32]X. A. Peng, J. Zhou, W. C. Wang, and D. P. Cao, Carbon **48**, 3760 (2010).
[33]S. S. Razavi, S. M. Hashemianzadeh, and H. Karimi, J. Mol. Model. **17**, 1163 (2011).
[34]S. Ban and C. Huang, J. Membr. Sci. **417**, 113 (2012).
[35]W. H. Zhao, B. Shang, S. P. Du, L. F. Yuan, J. Yang, and X. C. Zeng, J. Chem. Phys. **137**, 034501 (2012).
[36]P. Kowalczyk, Phys. Chem. Chem. Phys. **14**, 2784 (2012).
[37]L. Liu and S. K. Bhatia, J. Phys. Chem. C **117**, 13479 (2013).
[38]M. Rahimi, J. K. Singh, D. J. Babu, J. J. Schneider, and F. Müller-Plathe, J. Phys. Chem. C **117**, 13492 (2013).
[39]L. H. Lu, S. S. Wang, E. A. Müller, W. Cao, Y. D. Zhu, X. H. Lu, and G. Jackson, Fluid Phase Equilib. **362**, 227 (2014).
[40]M. Rahimi, D. J. Babu, J. K. Singh, Y. B. Yang, J. J. Schneider, and F. Müller-Plathe, J. Chem. Phys. **143**, 124701 (2015).
[41]M. Rahimi, J. K. Singh, and F. Müller-Plathe, Phys. Chem. Chem. Phys. **18**, 4112 (2016).
[42]J. J. Zhao, A. Buldum, J. Han, and J. P. Lu, Nanotechnology **13**, 195 (2002).
[43]D. Hedman, H. R. Barzegar, A. Rosén, T. Wågberg, and J. A. Larsson, Sci. Rep. **5**, 16850 (2015).
[44]M. P. Allen and D. J. Tildesley, *Computer Simulation of Liquids* (Clarendon Press, Oxford, 1987).
[45]D. Frenkel and B. Smit, *Understanding Molecular Simulation. From Algorithms to Applications*, 2nd ed. (Academic Press, London, 2002).
[46]J. J. Potoff and J. I. Siepmann, AIChE J. **47**, 1676 (2001).
[47]N. Hansen, F. A. B. Agbor, and F. J. Keil, Fluid Phase Equilib. **259**, 180 (2007).
[48]M. S. Dresselhaus, G. Dresselhaus, and R. Saito, Carbon **33**, 883 (1995).
[49]A. V. Vernov and W. A. Steele, Langmuir **2**, 219 (1986).
[50]M. J. Bojan and W. A. Steele, Langmuir **3**, 1123 (1987).
[51]E. J. Bottani, I. M. K. Ismail, M. J. Bojan, and W. A. Steele, Langmuir **10**, 3805 (1994).
[52]P. P. Ewald, Ann. Phys. **64**, 253 (1921).
[53]B. Widom, J. Chem. Phys. **39**, 2808 (1963).
[54]F. Karavias and A. L. Myers, Langmuir **7**, 3118 (1991).